Electronic Supplementary Material (ESI) for Journal of Materials Chemistry C.

Supplementary Information

The paradigm of the filler's dielectric permittivity and aspect ratio in high-*k* polymer nanocomposites for energy storage applications

Zouhair Hanani,[a,b,c,*] Daoud Mezzane,[a,d] M'barek Amjoud,[a] Mohammed Lahcini,[a] Matjaž Spreitzer,[c] Damjan Vengust,[c] Arash Jamali,[e] Mimoun El Marssi,[d] Zdravko Kutnjak[c] and Mohamed Gouné[b]

[a.] *IMED-Lab, Cadi Ayyad University, Marrakesh, 40000, Morocco*
[b.] *ICMCB, University of Bordeaux, Pessac, 33600, France*
[c.] *Jozef Stefan Institute, Ljubljana, 1000, Slovenia*
[d.] *LPMC, University of Picardy Jules Verne, Amiens, 80039, France*
[e.] *PME, University of Picardy Jules Verne, Amiens, 80039, France*

[*] *Corresponding author: e-mail: zouhair.hanani@ijs.si*

S1. Experimental procedures

S1.1. Materials

Polylactic acid (PLA) with reference Ingeo™ Biopolymer 6201D was purchased from NatureWorks. Titanium isopropoxide ($Ti[OCH(CH_3)_2]_4$, 97%), zirconium(IV) propoxide solution ($Zr[OCH_2CH_2CH_3]_4$, 70 wt.% in 1-propanol), zirconyl chloride octahydrate ($ZrOCl_2{\cdot}8H_2O$, 98%), isopropanol ($(CH3)_2CHOH$, ≥99.5%), barium acetate ($Ba(CH_3COO)_2$, 99%), calcium nitrate tetrahydrate ($Ca(NO_3)_2{\cdot}4H_2O$, 99%), glacial acetic acid (CH_3CO_2H, ≥99.7%), 2-methoxyethanol ($CH_3OCH_2CH_2OH$, 99.8%), cetyltrimethylammonium bromide (CTAB, $CH_3(CH_2)_{15}N(Br)(CH_3)_3$, ≥98%), sodium hydroxide (NaOH, ≥97.0%), hydrogen peroxide solution (H_2O_2, 30% (wt/wt) in H_2O), tris-HCl ($NH_2C(CH_2OH)_3{\cdot}HCl$, ≥99.0%), ethanol ($CH_3CH_2OH$, 96%), dichloromethane (CH_2Cl_2, ≥99.9%), methanol (CH_3OH, ≥99.8 %), and potassium bromide (KBr, ≥99% FT-IR grade), were purchased from Sigma Aldrich. Dopamine hydrochloride ($C_8H_{11}NO_2{\cdot}HCl$, 99%) was obtained from Alfa Aesar. Deionized water with a resistivity of 18.2 MΩ cm^{-1} was obtained from a PURELAB-classic water purification system (ELGA LabWater) and was used for the experiments conducted in this work.

S1.2. Electrical properties of PLA

Fig. S1 compares the electrical properties of some biodegradable polymers including PLA and some conventional polymers reported in,[1] and those of Solef® PVDF film (Solvay). The relative permittivities of biodegradable are comparable to those of conventional polymers (Fig. R1a), due to the presence of polar carbonyl and hydroxyl groups in their structures.[2] PLA shows a relative permittivity around 3, closer to some conventional polymers used in electrical cables like PE and PP, and very far from PVDF. Despite the biodegradable polymers exhibit high value of losses, PLA has the lowest level of dissipation factor (Fig. R1b) and exhibits low dielectric loss as compared to PVDF and epoxy resin. Concerning the apparent conductivity, only PLA could be argued for competing with classical polymers like LDPE and PVDF (Fig. R1c). The rest of the biodegradable polymers shows high level of apparent conductivity. The DC breakdown strength of PLA is higher than all other biodegradable polymers and even high compared to some conventional polymers like LDPE and PVDF (Fig. R1d). According to these results, the electric properties PLA are enhanced compared to other biodegradable polymers, and even it can compete conventional polymers like LDPE and PVDF. which make it very promising biopolymer

for the fabrication of ceramic/polymer nanocomposites for electrical insulation and energy storage applications.

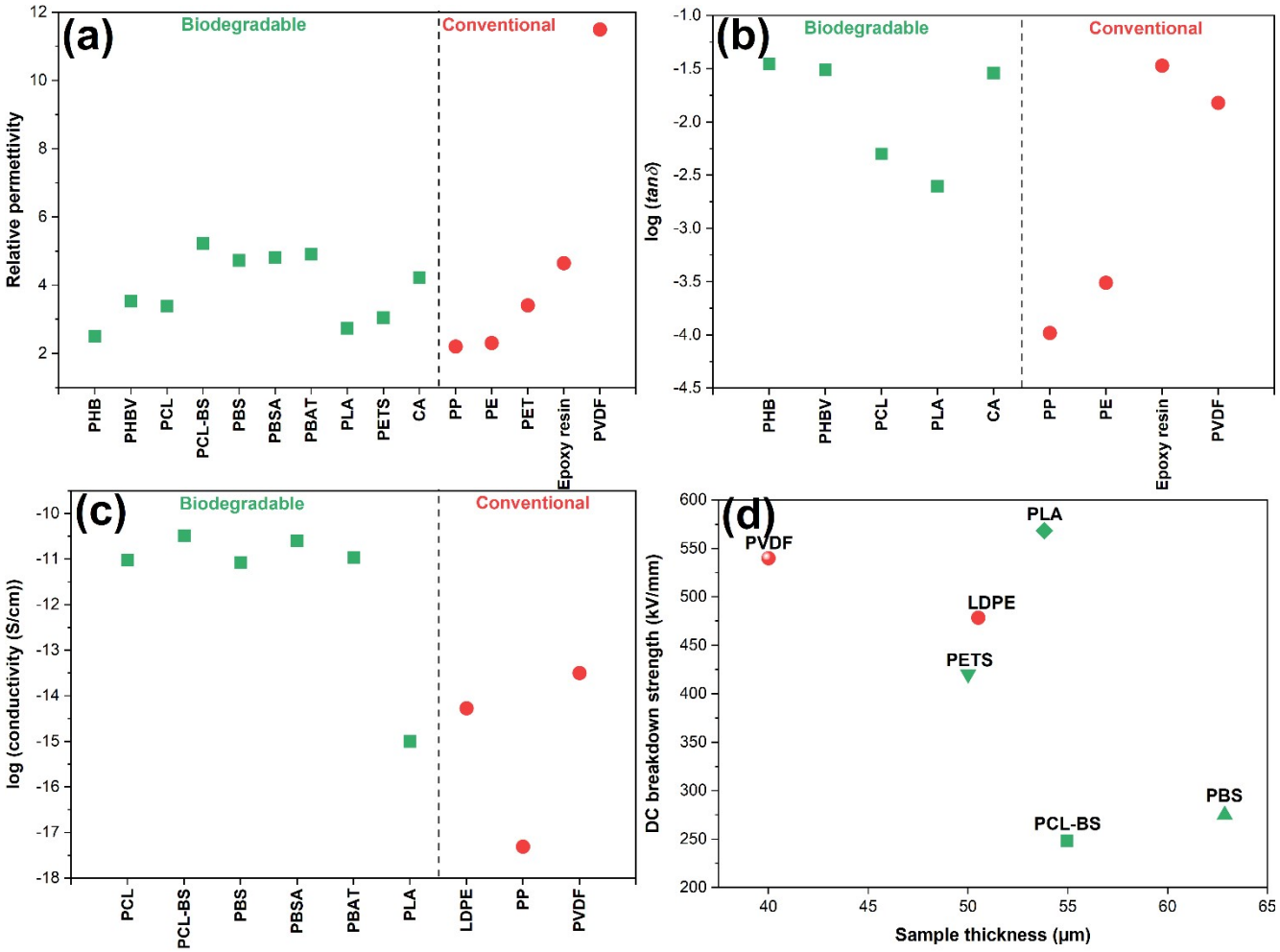

Fig. S1 Electrical properties of some biodegradable and conventional polymers. (a) relative permittivity, (b) loss tangent, (c) apparent conductivity and (d) DC breakdown strength.[1]

S1.3. Elaboration of B_NP, HZTO_NW and B_NR powders

BCZT spherical particles (B_NP)

BCZT nanocrystalline and pure powder with spherical-shape was obtained through a sol-gel method followed by a single-step hydrothermal synthesis in a high alkaline medium at 160 °C for 24 h as reported in.[3] First, under inert atmosphere (N_2), appropriate amounts of titanium isopropoxide and zirconium n-propoxide were mixed with isopropanol. After 1 h of vigorous stirring, deionized water was added into the solution dropwise to produce a gel designated ZTO. This was washed several times and dried at 80 °C for 12 h to obtain ZTO powder. Next, a stoichiometric quantity of ZTO powder was dispersed in 100 mL of NaOH (10 M) solution for 1 h. Meanwhile, calcium nitrate tetrahydrate and barium acetate were dissolved in 50 mL of

deionized water. Then, the two solutions were mixed together in a 250-ml round-bottom flask equipped with a magnetic stirrer for 3 h under nitrogen flow. After, the suspension obtained was transferred to a Teflon-lined stainless-steel autoclave, purged with nitrogen, sealed and heated at 160 °C for 24 h. After the reaction was completed, the sealed autoclave was cooled down to room temperature. The resulting white precipitate was collected by centrifugation at 12000 rpm for 10 min, and washed several times with distilled water and ethanol. Then, the final product was dried at 100 °C for 12 h.

HZTO nanowires (HZTO_NW)

$H_2(Zr_{0.1}Ti_{0.9})_3O_7$ nanowires (HZTO_NW) were produced by hydrothermal processing in high alkaline medium at 240 °C for 48 h as reported in.[4] The $Zr_{0.1}Ti_{0.9}O_2$ (ZTO) powder, synthesized as described elsewhere,[5] was dispersed in 100 mL of 10 M NaOH aqueous solution. After 1 h of stirring, the suspension was transferred to a 150 mL-Teflon-lined stainless-steel autoclave, sealed and heated to 240 °C with 48 h dwell time, then cooled down to room temperature. The resulting white suspension ($Na_2(Zr_{0.1}Ti_{0.9})_3O_7$, NaZTO) was collected by filtration and soaked in 0.2 M HCl solution for 10 h to convert NaZTO to HZTO. The latter was washed several times with deionized water and ethanol using repeated centrifugation at 4000 rpm for 10 min until reaching the neutrality of the medium (pH=7). The filtered HZTO_NW were redispersed in deionized water by mechanical stirring at 60 rpm for 30 min, then freeze-dried for 48 h to obtain a fluffy product.

BCZT rod-like (B_NR)

BCZT rod-like powder with rod-like particles (B_NR) was obtained by surfactant-assisted solvothermal synthesis at 180 °C for 12 h and 30 mM of cetyltrimethylammonium bromide (CTAB) surfactant, as reported in.[6] First, an appropriate amount of barium acetate was dissolved in glacial acetic acid. Calcium nitrate tetrahydrate and zirconyl chloride octahydrate were dissolved each alone in 2-methoxyethanol. Second, the three solutions were mixed in a two-neck round bottom flask. Then, titanium isopropoxide was added synchronously dropwise to the reaction medium using an isobaric dropping funnel. Afterward, to control BCZT microstructure, 30 mM of CTAB surfactant was introduced. The obtained solution was transferred to a 30 mL-Teflon-lined stainless-steel autoclave at 180 °C in an oven for 12 h. After the reaction was completed, the sealed autoclave was cooled in the air. The resulting product was washed sequentially with ethanol for several times. Then, the final product was dried at 100 °C for 12 h, calcined at 1000 °C for 4 h.

S1.4. Functionalisation of BCZT nanoparticles (B_NP)

To enhance chemical interactions between BCZT nanoparticles and the PLA matrix, the surface of the nanoparticles was pre-treated. Fig. S2a displays the different processes during the functionalisation of B_NP nanoparticles. The B_NP powder was first dispersed in the hydrogen peroxide solution by ultrasound for 30 min and then refluxed at 104 °C for 4 h. The obtained hydroxylated product (B_NP-OH) was recovered by centrifugation at 12000 rpm for 10 min, washed several times with demineralised water and ethanol and then dried under vacuum at 80 °C for 12 h. Subsequently, the hydroxylated B_NP nanoparticles were coated with a PDA shell by air oxidation of dopamine, to form B_NP@PDA according to the reaction in Fig. S2b. For that purpose, 2 g of the B_NP powder was dispersed in 100 ml of the Tris-HCl (10 mM) by ultrasound for 15 min. The pH of the dopamine (DA) aqueous solution was buffered to 8.5 by adding the 10 mM Tris-HCl. After 24 h of reaction at reflux at 60 °C, a black powder B_NP@PDA was recovered by centrifugation at 12000 rpm for 10 min, washed several times with demineralised water and ethanol, then dried at 80 °C for 24 h.

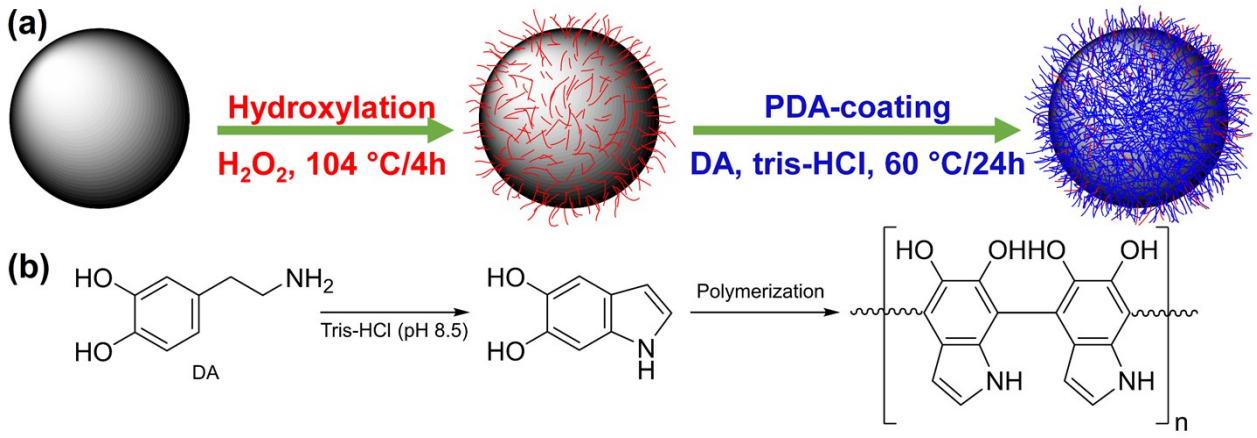

Fig. S2 (a) Schematic illustration of the preparation of core–shell structured B_NP@PDA nanofillers and (b) the polymerisation reaction of dopamine.

S1.5. Elaboration of PLA-based nanocomposite films

First, 10 g of PLA beads was purified by several solubilisation/precipitation (recrystallisation) cycles in dichloromethane and methanol, respectively, followed by drying in vacuum at 50 °C for 12 h. Then, PLA-based nanocomposite films were elaborated by the solution casting method using the volume fractions 3, 6, 10, 15 and 20 vol% of B_NP, B_NP@PDA, HZTO_NW and B_NR fillers. Specifically, an adequate amount of PLA was solubilised in dichloromethane with magnetic stirring for 2 h. Then, an appropriate mass of the fillers was dispersed therein, by

ultrasound for 15 min, then homogenised by magnetic stirring for another 2 h. The slurry was cast in a Teflon petri dish and then dried at room temperature to obtain a flexible composite film, and finally dried in vacuum at 40 °C for 12 h to remove solvent. The thickness of the films was found to be between 15 and 40 microns.

S1.6. Characterisations

Fourier transform infrared spectroscopy (FT-IR) was used to monitor the functionalisation of BCZT nanoparticles starting with the BCZT powder, hydroxylation, through polydopamine coating and to follow the incorporation of B_NP and B_NP@PDA nanoparticles into the PLA matrix. KBr pellet was prepared by using a manual press for the background spectrum. In the case of B_NP and B_NP@PDA nanoparticles, 1 wt% of previously dried sample under vacuum at 80 °C for 6 h was homogeneously mixed with KBr for spectroscopic measurement. In contrast, PLA and PLA-based nanocomposite films were dried in vacuum at 50 °C for 6 h. The spectrum was recorded by using a Bruker Optics Vertex 70 spectrometer in the range of 4000–450 cm^{-1} with a resolution of 4 cm^{-1} (at 32 scans). Thermogravimetric analysis (TGA) was used in order to determine the weight percentage of the PDA coating in the B_NP@PDA structure. A Discovery Series TGA 55 (TA instruments) device was used to characterise the thermal transformations occurring in the products during the heating process. About 8 mg of the sample was placed in a platinum pan and heated from the room temperature to 800 °C at a heating rate of 10 °C min^{-1} and under a nitrogen flow of 40 ml min^{-1}. A transmission electron microscope (TEM, JEOL – ARM 200F Cold FEG TEM/ STEM) operating at 200 kV, equipped with a spherical aberration (Cs) probe and image correctors with point resolution 0.12 nm, was used to observe the morphology of the BCZT powder, and to visualise the thickness of PDA coating on the surface of BCZT nanoparticles when coupled with a High-Angle Annular Dark-Field (HAADF) detector. The dispersion of B_NP/PLA, B_NR@PDA/PLA, HZTO_NW/PLA and B_NR/PLA nanofillers in the PLA matrix at the surface and at the cross-section of the nanocomposite film was observed by using a Field-Emission Scanning Electron Microscope (FESEM, JEOL 7600F). The average thicknesses of the nanocomposite films were measured by a precise coating thickness gauge (Surfix Pro S, Phynix). The dielectric properties of gold-sputtered PLA-based nanocomposite films were determined by a precision LCR Meter (Hioki, IM 3570) in the frequency range of 100 Hz to 1 MHz at room temperature. The theoretical calculations of the effective dielectric permittivity were performed using Fortran software. The ferroelectric hysteresis loops were recorded at a

driving frequency of 100 Hz by a ferroelectric test system (AiXACCT, TF Analyzer 3000) equipped with a high voltage amplifier (Trek, 2220).

S2. Results and discussions

S2.1. Structural properties of BCZT/PLA nanocomposites

The STEM–HAADF micrographs of Fig. S3a, b evidence the successful coating of the B_NP nanoparticles by PDA with a shell thickness about 15–25 nm. Meanwhile, Fig. S3c exhibits TGA data of the weight changes of B_NP and B_NP@PDA nanoparticles. The first weight loss between 30 °C to 150 °C is due to dehydration (adsorbed water). The second loss between 150 °C and 500 °C corresponds to the thermal decomposition of various organic compounds including the PDA layer. Above 500 °C the weight loss for both compounds remains constant. The total weight loss is 6.13% and 9.95% for B_NP and B_NP@PDA, respectively. The weight percentage of the functional PDA layer was obtained by comparison of the B_NP and B_NP@PDA TGA data. Based on the total weight loss values, the mass percentage of the PDA coating layer is approximately 3.82 wt%, which prove the effective modification of B_NP nanoparticles in this work.

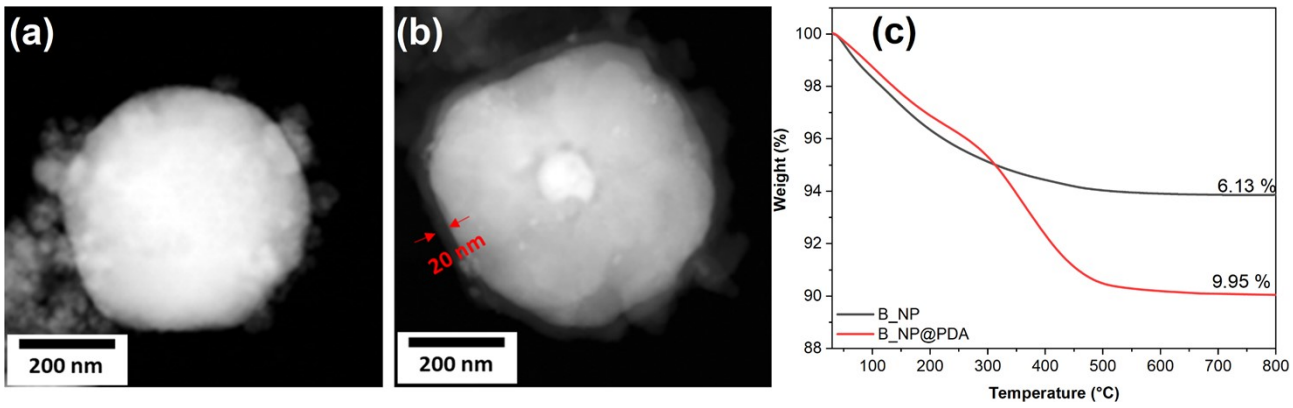

Fig. S3 Core-shell structuration of B_NP nanoparticles. STEM–HAADF micrographs of (a) B_NP nanoparticle, (b) B_NP@PDA nanoparticle showing PDA layer thickness with the red lines) and (c) TGA curves of B_NP and B_NP@PDA nanoparticles.

It has been reported that the surface of barium titanate based powders contain hydroxyl groups (−OH),[7,8] however, the content of −OH groups is too low to have a significant impact on the surface reactivity with the dispersants. Therefore, the hydroxylation of the particles surface is important precondition for effective functionalisation of B_NP nanopowders.[9] Fig. S4a shows

a superposition of infrared spectra of B_NP powders before and after hydroxylation with hydrogen peroxide (H_2O_2). After treatment of the powder, a broad absorption band, due to the elongation vibrations of the MO−H groups (M stands here for Ba, Ca, Zr and Ti), is observed at around 3440 cm^{-1} and confirmed by the increasing intensity of the absorption band M−O and/or deformation outside the plane of the OH groups, situated between 500 and 650 cm^{-1}. This highlights the successful functionalisation of B_NP surface by hydroxyls groups to form B_NP−OH nanoparticles. Moreover, Fig. 3a depicts the surface functionalisation of B_NP−OH by PDA layer. The observed peaks ranging from 1060 cm^{-1} to 1200 cm^{-1} refer to the bond −C≡N of secondary amine,[10] and the peak at 1380 cm^{-1} is assigned to the phenolic C−O−H vibration.[11] In addition, the absorption peaks at wavenumbers of 1630, 1490, 1265 and 1100 cm^{-1} correspond to the vibrations of the N−H, C=C, C−N and C−O bonds, respectively.[12] The broad peak centred at 3430 cm^{-1} is attributed to the vibrations of aromatic C−H bonds, N−H amine bonds and non-functionalised −O−H groups. The increasing peaks from 3000 cm^{-1} to 3680 cm^{-1} correspond to the bond of −OH and −NH− of coated PDA.[10] Infrared spectroscopy was also used to confirm the success of the B_NP@PDA/PLA preparation. Fig. S4b shows the FTIR spectra of PLA and B_NP@PDA/PLA nanocomposite films. It can be seen that a new peak at 1760 cm^{-1} appeared in the infrared spectra of B_NP@PDA/PLA, which is attributed to C=O stretching vibrations of the PLA ester groups. In addition, new absorption bands were also found at 1190–1110 cm^{-1}, indicating the symmetric, stretching-vibration C−O−C groups of the PLA and also the appearance of the broad M−OH peak around 3440 cm^{-1} due to the functionalisation of the surface of the loads.[13,14]

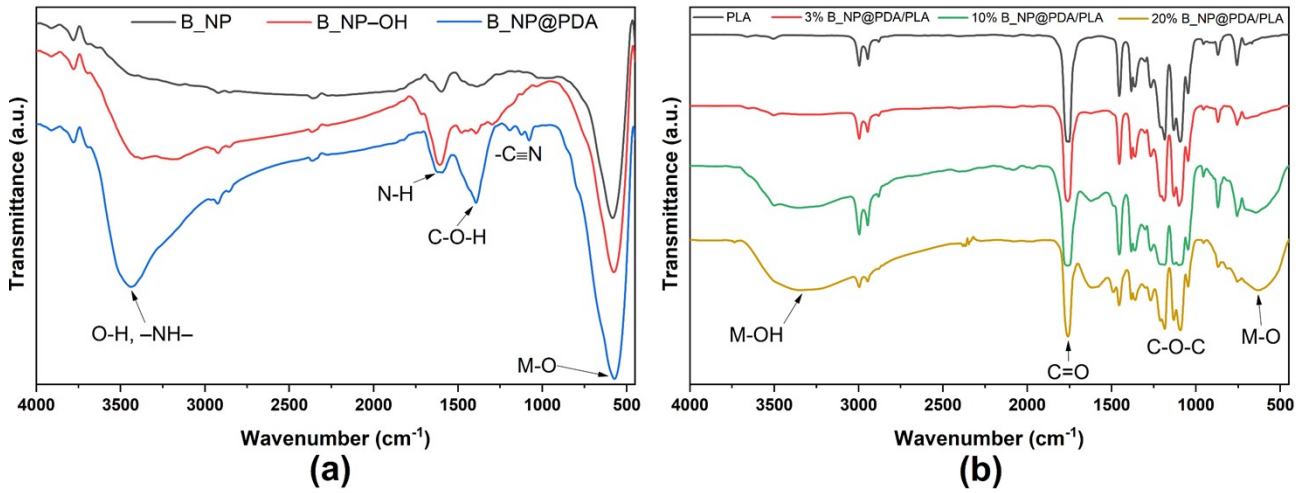

Fig. S4 FTIR patterns of (a) B_NP, B_NP–OH, B_NP@PDA nanoparticles and (b) B_NP@PDA/PLA films.

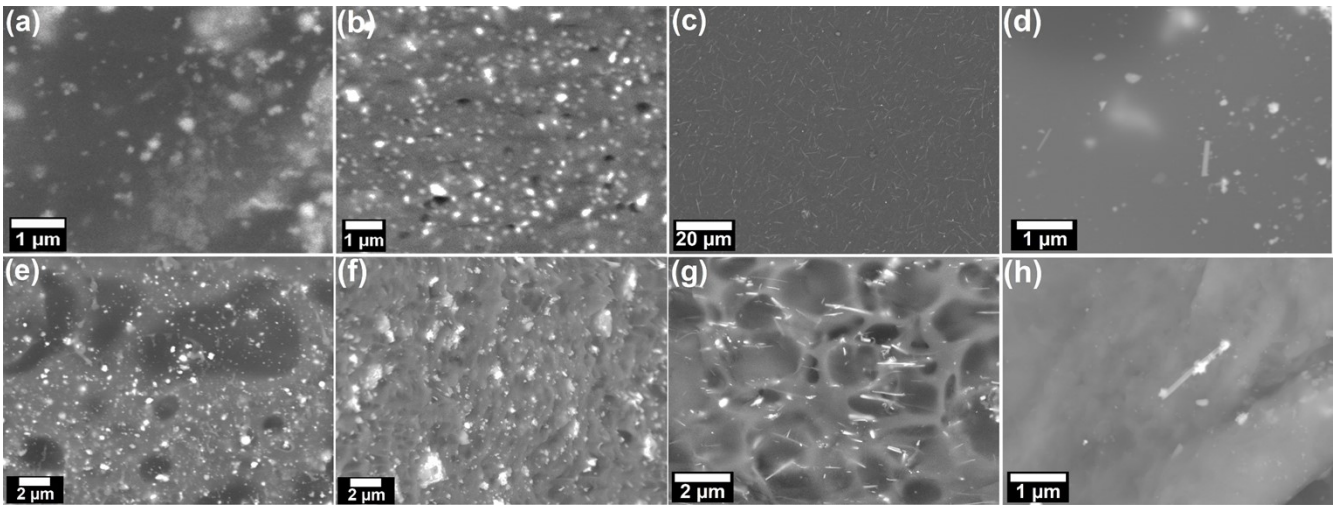

Fig. S5 Morphological properties of the PLA-based nanocomposite films after dispersing 3 vol% of nanofillers in PLA matrix. FESEM images at surface (a–d) and at the cross-section (e–h) of B_NP/PLA, B_NP@PDA/PLA, HZTO_NW/PLA and B_NR/PLA nanocomposite films, respectively.

S2.2. Dielectric and energy storage properties of the PLA-based nanocomposites

The room-temperature frequency-dependencies of the dielectric permittivity (ε_r) and the dielectric loss ($tan\ \delta$) of B_NP/PLA, B_NR@PDA/PLA, HZTO_NW/PLA and B_NR/PLA nanocomposites films with different volume fractions measured under the frequency ranging from 100 Hz to 1 MHz are shown in Fig. S6. Not surprisingly, an increase of ε_r and $tan\ \delta$ is highlighted for all the nanocomposites in comparison to the pure PLA. The values of ε_r decrease gradually with increasing frequency. This effect, even stronger that the volume fraction of charges is large, can be explained by interfacial polarisation, i.e., by Maxwell-Wagner-Sillars (MWS) effect.[15,16] At low frequency, the fillers exhibit well defined conducting grains separated by thin insulating grain boundaries, which causes accumulation of charges under the influence of the electric field and thus increasing the interfacial polarisation resulting in a higher dielectric permittivity. However, at higher frequencies, the charge carriers cannot align themselves in the direction of the electric field resulting in a reduced interfacial polarisation and leading in a lower dielectric permittivity at high frequencies.[17] The charges stored within the nanocomposites would possibly be delocalised either by tunnelling or by ohmic conduction leading to fairly high loss factors.[18] Compared to the nanocomposites with spherical inclusions (B_NP and B_NP@PDA), the nanocomposites loaded with high aspect ratio nanofiller (HZTO_NW and B_NR) possess a remarkably improved dielectric permittivity although the permittivities of HZTO_NW and B_NR is lower than the one of B_NP (see Table 1 for comparison). At 1 kHz and

by using 20 vol% of nanofillers, the dielectric permittivities of the HZTO_NW/PLA and B_NR/PLA nanocomposites films reach 16.00 and 20.28, respectively, which are higher than those of B_NP/PLA (ε_r=9.11) and B_NP@PDA/PLA (ε_r=11.24). Meanwhile, Fig. S6e–h display that *tan δ* of all nanocomposite films. A decrease of *tan δ,* due to interfacial polarisation, was observed up to a critical frequency (around 70 kHz), followed by a sharp increase attributed to the dipole polarisation relaxation in PLA.[19] decreases at first and then increases with frequency. By increasing the nanofillers content, *tan δ* of all nanocomposite films is inescapably amplified. It is worth noting that even at high nanofiller loads, the two types of nanocomposite films, do not show a high *tan δ* at a wide frequency range.

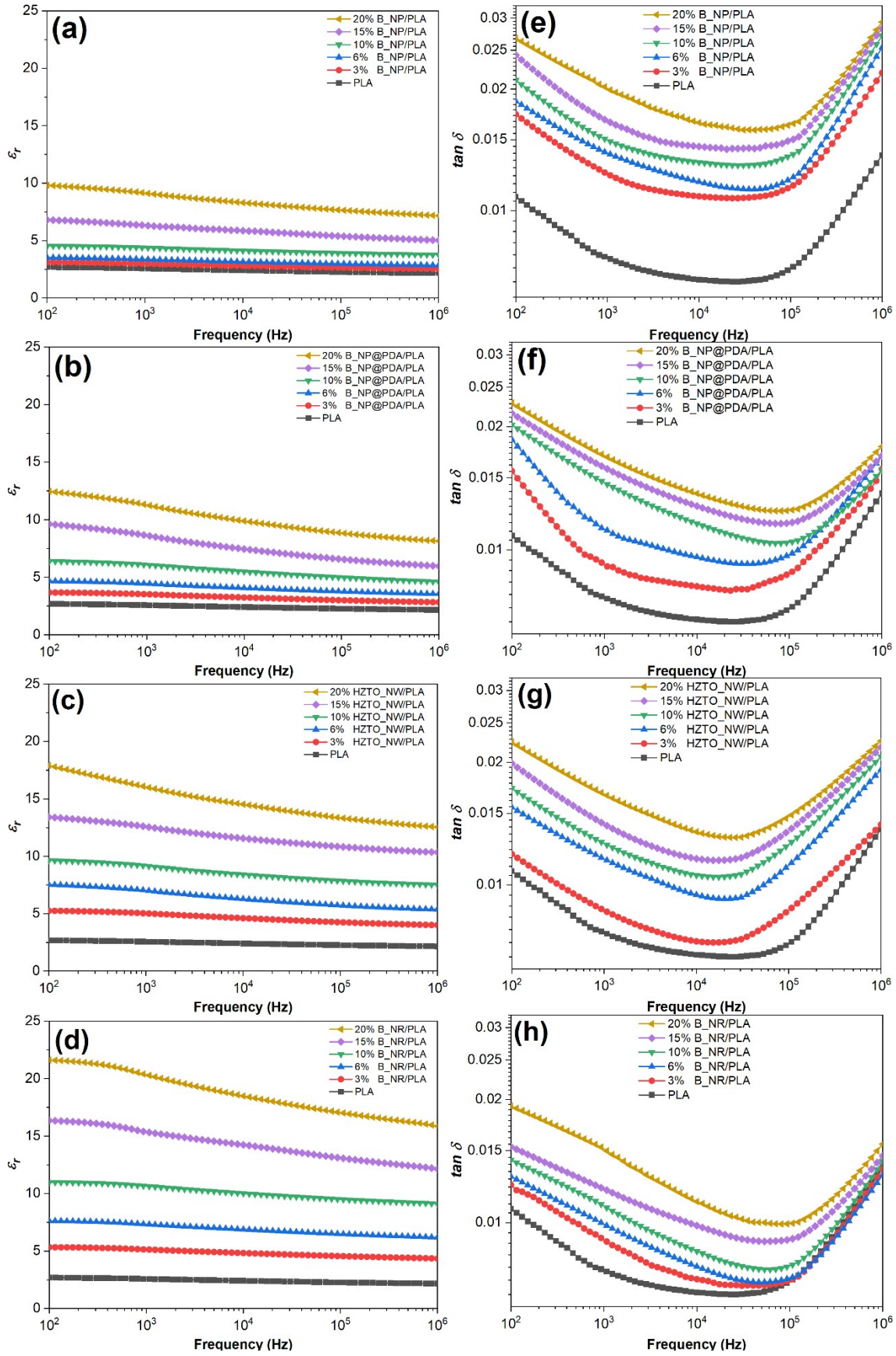

Fig. S6 The dielectric properties of the PLA-based nanocomposites. (a–d) ε_r and (e–h) *tan δ* of B_NP/PLA, B_NP@PDA/PLA, HZTO_NW/PLA and B_NR /PLA nanocomposites, respectively.

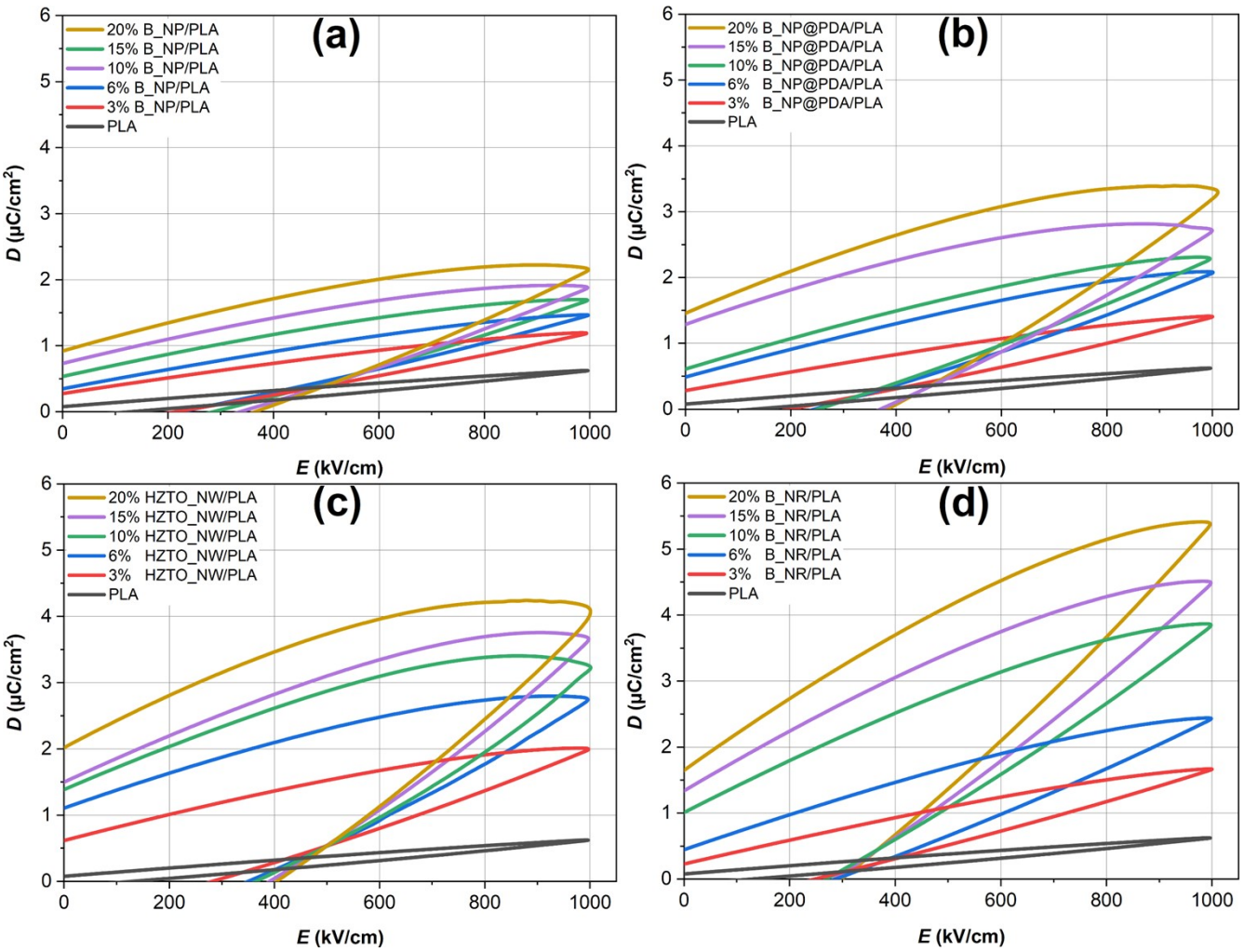

Fig. S7 Energy storage performances of the PLA-based nanocomposites. *D*–*E* loops of (a) B_NP/PLA, (b) B_NP@PDA/PLA, (c) HZTO_NW/PLA and (d) B_NR/PLA nanocomposites.

S2.3. Effects of both volume fraction and aspect ratio of fillers on the effective permittivity of the nanocomposite: quantitative analysis

Fig. S8 gives the comparison between the effective permittivities measured and those obtained from the so-called Wiener bounds as a function of B_NP volume fraction and for different values of B_NP permittivity (100, 1000 and 10000).[20] The lower-bound and the upper-bound are given by the following equations, and correspond to capacitors that are connected in parallel or series in a circuit.

$$\begin{cases} (\varepsilon_{eff})_{Inf} = \dfrac{\varepsilon_c \varepsilon_p}{f_c \varepsilon_c + (1 - f_c)\varepsilon_p} \\ (\varepsilon_{eff})_{Sup} = f_c \varepsilon_c + (1 - f_c)\varepsilon_p \end{cases} \qquad \text{(Eq. S1)}$$

It can be seen that the Wiener bounds depend on the set of permittivity and the volume fraction but not directly on the exact geometry of the mixture. Also, these bounds are known to be less restrictive than others such as Hashin–Shtrickman bounds.[21] Whatever the value of B_NP permittivity considered; the effective permittivity of the mixture is located between the Wiener bounds. This is not surprising since these bounds can be considered as absolute limits. However, it is worth noting that the lower bound characterises a system in which the presence of ceramic inclusions does not influence the effective permittivity of the mixture up to a very high-volume fraction of ceramic (of about 70 vol%). In other words, the polarisation induced by the presence of inclusions in the mixture can be considered as negligible. Our experimental data are located above the lower bound and show clearly an increase of effective permittivity from 2.6 to 8.6 for the B_NP/PLA (and 11.6 for the B_NP@PDA/PLA) within the B_NP volume fraction range of 0 to 20 vol%. This highlights a change in the macroscopic electrical field inside the medium as a function of B_NP volume fraction.

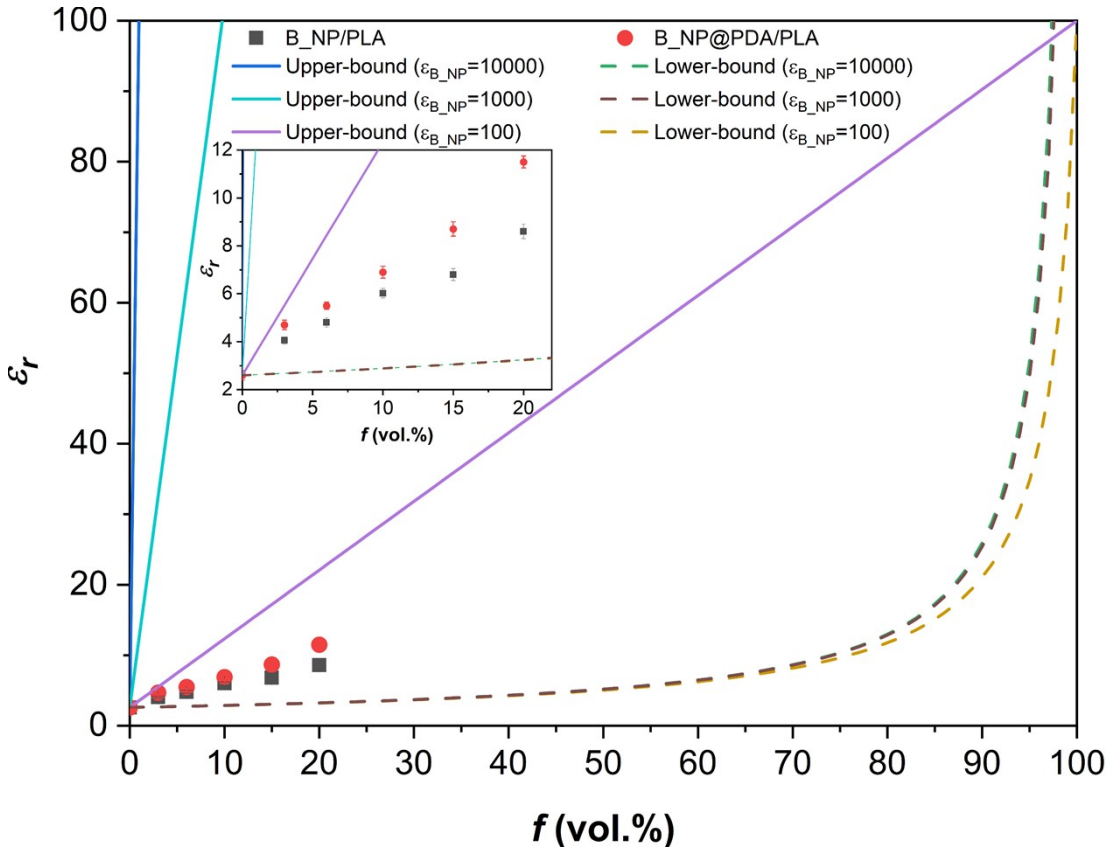

Fig. S8 Evolution of the effective permittivity of the B_NP/PLA and B_NP@PDA/PLA composites as a function of volume fraction of B_NP as inclusion. Comparison with the lower and upper Wiener bounds defined from different value of the B_NP permittivity.

Although the increase of the effective permittivity measured is relatively high (multiplied on average by 4 between 0 and 20 vol% of B_NP in the composites), it remains weak in comparison with the expected high value of near-spherical B_NP permittivity. Furthermore, the effective permittivity of the composite evolves linearly between 0 and 20 vol% of B_NP. This type of behavior was also highlighted in the case of TiO_2/epoxy composite for volume fractions of TiO_2 below 35 vol%.[22] An extrapolation of this trend to 100 vol% of B_NP would give a permittivity of about 40 for the B_NP permittivity, a too low value when compared to the value of 12085 as sintered.[23] As a result, a sharp increase of permittivity is expected from a critical volume fraction of B_NP. This behavior can be interpreted from the work of Cheng et al. and on the basis of a numerical three-dimensional "disordered model".[24] It is based on finite element method (FEM) and takes into account the interconnection of inclusions when concentration of inclusions is increased. It is thus a powerful method to study the effects of both the permittivity contrast between ceramic as inclusion and polymer as matrix and the interconnection (or percolation) of ceramic particles into the polymer matrix. The dielectric properties obtained by the "disordered model" were compared to those of the periodic models and the classical analytical mixture rules. From this study, we can draw some important learning points. First, if the permittivity contrast is close to one, all the models are equivalents and the composite behaves as dilute mixture i.e., the effective permittivity evolves linearly with the volume fraction of the ceramic particles. Second, a deviation was observed when the permittivity contrast becomes larger. As it increases, the periodic and the Maxwell-Garnett models fail to describe the reliable effective permittivity.[25] The Maxwell rule is based on the assumption of spherical inclusions of mean distance much larger than their radius. In other words, it cannot be applied for high volume fraction of particles (>10 vol%). The fact that periodic models fail show indirectly that arrangement of particles play a role in resulting effective permittivity; especially in the case of high permittivity contrast. Finally, in all cases and even for large contrast between inclusions and matrix, it is shown that below a critical volume fraction that depends on the model considered, the effective permittivity shows a linear dependence with the volume fraction of inclusions.[24] This can be simply explained by the fact that the domains are spatially separated and electrostatic interactions between each inclusion and its neighbours are relatively weak. For instance, the "disordered model" shows that the effective permittivity evolves linearly with the volume fraction of inclusions up to a critical volume fraction of around 20 vol%; a value close to our observations. In order to go further, we have decided to apply the model developed by.[26]

It has Maxwell-Garnett (MG) equation as a low volume filling ratio limit and Bruggeman Symmetrical (BS) equation as a high-volume filling ratio limit. When the volume fraction of inclusions increases, the local electric field acting on each inclusion approaches a similar field as in the BS mixing equation. This model was chosen since it was derived especially for composites with high electrical contrast between the inclusions and the background phase, inclusions are allowed to overlap and is valid for both spherical and ellipsoidal inclusions. The result is the following differential equation for the unknown effective permittivity and applicable for spherical shape of B_NP:

$$\frac{d\varepsilon_{eff}}{df} = \frac{\varepsilon_{PLA}(\varepsilon_{B\_NP} - \varepsilon_{PLA})}{\varepsilon_{B\_NP} + 2\varepsilon_{eff} - 3f\varepsilon_{PLA}} \qquad \text{(Eq. S2)}$$

It was solved numerically and the effect of B_NP permittivity on the effective permittivity of the composite was calculated and compared to experimental results in Fig. 5.

Many interesting conclusions may be drawn. First, an abrupt change of the effective permittivity, even stronger than the electrical contrast between B_NP and PLA is high, was observed from a critical volume fraction of $\frac{1}{3}$. This value represents the depolarisation factor in the case of spheres introduced into the model to describe how the polarisation is affected by both the shape and the orientation of inclusions with respect to the applied field (see Eq. (S3) and Eq. (S4)). It also corresponds to the percolation threshold (f_c) of spheres randomly distributed. Second, below the percolation threshold and as observed experimentally, the effective permittivity increases linearly with both increasing volume fraction and permittivity of B_NP. However, from a critical value of permittivity around 100 (that corresponds to a dielectric mismatch of $\frac{100}{2.7} = 37)$, the effective permittivity no longer evolves. In other terms, when spherical inclusions do not touch each other, there is a critical permittivity of B_NP from which the effective permittivity does not increase even for giant permittivities of B_NP ceramic. This can be explained by solving Laplace equation for a sphere embedded in an infinite host. Indeed, under these assumptions, the polarisability α and the depolarisation field generated by the polarised matter inside the inclusion E_{dep} are given by the following equations:[27]

$$\alpha = a^3 \varepsilon_{PLA} \frac{\varepsilon_{B\_NP} - \varepsilon_{PLA}}{\varepsilon_{B\_NP} + 2\varepsilon_{PLA}} \qquad \text{(Eq. S3)}$$

$$E_{dep} = - E_{ext}\left(\frac{\varepsilon_{B\_NP} - \varepsilon_{PLA}}{\varepsilon_{B\_NP} + 2\varepsilon_{PLA}}\right) \quad \text{(Eq. S4)}$$

where a is the mean radius of the B_NP inclusions, ε_{B_NP} and ε_{PLA} are the permittivity of B_NP ceramic and PLA polymer respectively and E_{ext} is the external field. The minus sign added indicates that the external field is counteracted by the depolarisation field.

The internal field E_{int} inside the inclusions which is considered as uniform according to the weak Eshelby conjecture,[28] can be rewritten from[27] as follow, since $E_{int}=E_{ext}+E_{dep}$ (where E_{dep} is the depolarisation field).

$$E_{int} = E_{ext}\left(1 - \frac{\varepsilon_{B\_NP} - \varepsilon_{PLA}}{\varepsilon_{B\_NP} + 2\varepsilon_{PLA}}\right) \quad \text{(Eq. S5)}$$

It is thus interesting to plot $\frac{\alpha}{a^3}$ and $\frac{E_{int}}{E_{ext}}$ as a function of ε_{B_NP} for a value of ε_{PLA}=2.7. The results obtained are given in Fig. S9a, b, respectively.

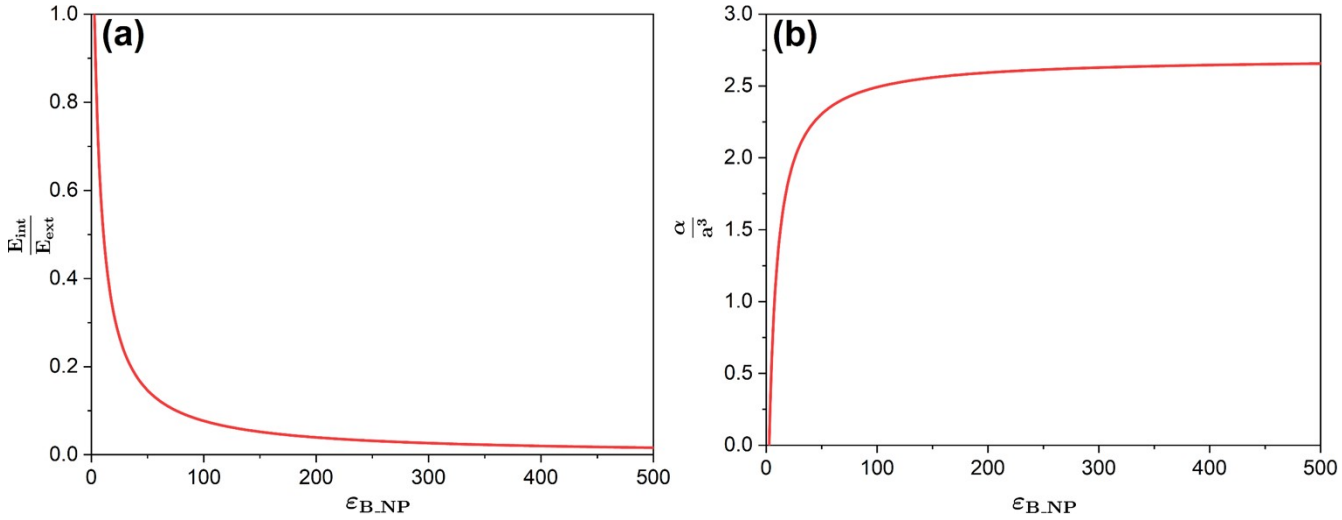

Fig. S9 (a) Evolution of the internal field E_{int} (via the ratio $\frac{E_{int}}{E_{ext}}$) as a function of the B_NP permittivity. (b) Evolution of the polarizability α (via the ratio $\frac{\alpha}{a^3}$) as a function of the B_NP permittivity.

S2.4. Effects of the aspect ratio of fillers on the effective permittivity of the nanocomposite: quantitative analysis

As explained before, the morphology of the dispersed B_NP ceramic can have an influence on the effective permittivity of the composites. In order to study this effect, we have decided to adapt the model developed to a mixture of randomly oriented ellipsoids of B_NP ceramic into PLA matrix. In that case, the differential equation used for spherical particles must be modified as follow:[26]

$$\frac{d\varepsilon_{eff}}{df} = \varepsilon_{PLA}\left(\varepsilon_{B\_NP} - \varepsilon_{eff}\right) \frac{\sum_{j=x,y,z} \left(\varepsilon_{eff} + N_j(\varepsilon_{B\_NP} - \varepsilon_{eff})\right)^{-1}}{3 - f\varepsilon_{B\_NP} \sum_{j=x,y,z} \left(\varepsilon_{eff} + N_j(\varepsilon_{B\_NP} - \varepsilon_{eff})\right)^{-1}} \quad \text{(Eq. S6)}$$

where N_j are the depolarisation factors in the three directions of space *x*, *y* and *z*, also known as the geometrical factors of electrostatics. More precisely, they represent the diagonal components of a tensor that can interpreted as a generalised depolarising dyadic of a particle. Assuming the spheroid *z* axis be the rotational axis, we have for prolate particles:[29]

$$N_z = \frac{1 - e^2}{e^3}(\text{arctanh}\,(e) - e) \quad \text{(Eq. S7)}$$

where *e* is the eccentricity. The prolate spheroid ranges from a needle (*e*=1) to a sphere (*e*=0). The hyperbolic arctan can be expressed as:

$$\text{arctanh}\,(e) = \frac{1}{2} ln \frac{1 + e}{1 - e} \quad \text{(Eq. S8)}$$

For a prolate, the following expression must be used:

$$e = \sqrt{\frac{\left(\frac{c}{a}\right)^2 - 1}{\left(\frac{c}{a}\right)^2}} \quad \text{(Eq. S9)}$$

where $\frac{c}{a}$ is the aspect ratio of particles.

The remaining depolarisation factors N_x and N_y can be determined by using the sum rule: N_x=N_y=N_z=1. We thus obtain the following relations:

$$\begin{cases} N_x = \frac{1}{2}(1 - N_z) \\ N_y = \frac{1}{2}(1 - N_z) \end{cases} \quad \text{(Eq. S10)}$$

Ultimately, the depolarisation factors take into account that the polarisability induced by the presence of particles into composite is a function of the inclusion geometry and orientation with respect to the applied electrical field.

Eq. (6) was solved numerically and the main results were given in Fig. 6 and Fig. S10. In Fig. 6, the effects of B_NP ceramic aspect ratio on the effective permittivity of the composite was highlighted. For a given permittivity of B_NP of 10000, increasing the aspect ratio of B_NP ceramic leads to an increase of the effective permittivity of the composite. The reason for this is that the induced polarisability is enhanced with the aspect ratio. Indeed, the average response of one ellipsoid is the sum of its three polarisability components:[30]

$$\alpha = \frac{1}{3}\sum_{x,y,z} \frac{\varepsilon_{B\_NP} - 1}{1 + N_i(\varepsilon_{B\_NP} - 1)} \quad \text{(Eq. S11)}$$

The polarisability induced by the major axis of the spheroid increases strongly with increasing eccentricity and aspect ratio.

Another possible and complementary way to think is to consider the effect of aspect ratio on the percolation threshold. Fig. 6 shows a rapid increase of effective permittivity at a given volume fraction of B_NP that depends on the aspect ratio. All happen as if the effective permittivity is strongly enhanced at a volume fraction that corresponds to the percolation threshold. In other word, the model developed reflect also the aspect ratio dependence of the percolation threshold (f_c) (see Fig. S10).

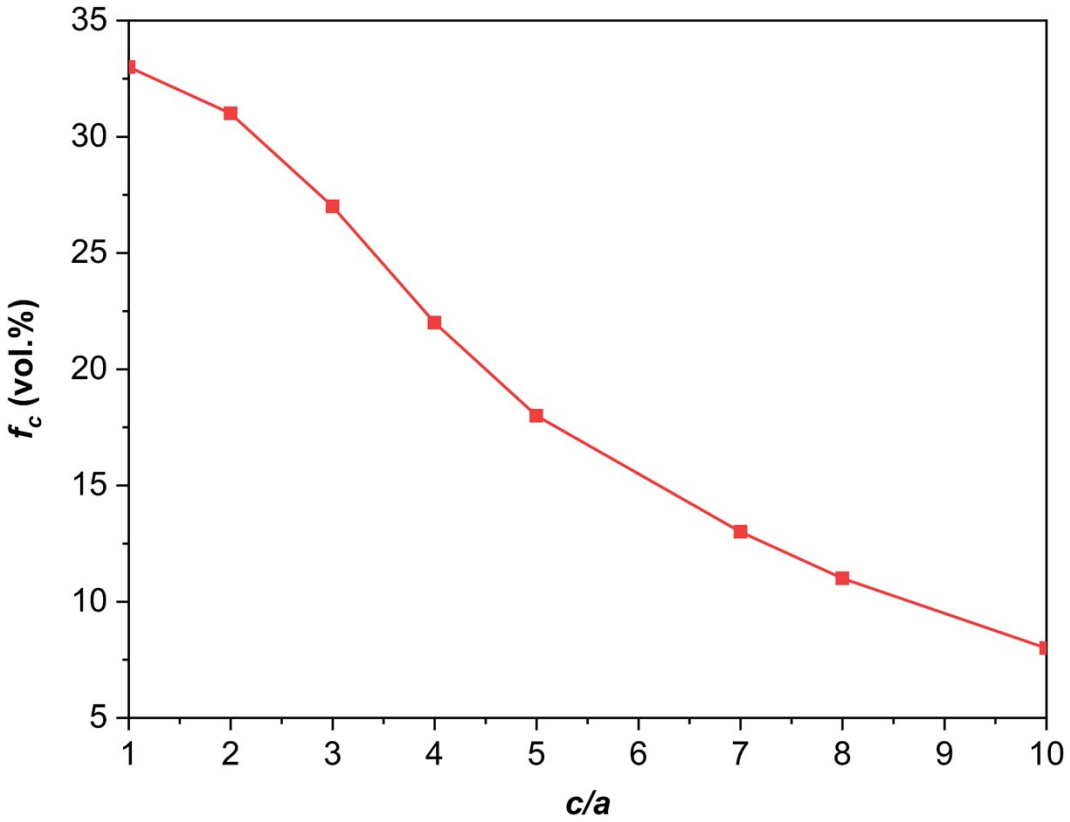

Fig. S10 Calculation of the evolution of the percolation threshold of B_NP into PLA as a function the aspect ratio of B_NP.

References

1 V. Hegde, 2017.

2 Y. Ohki and N. Hirai, in *Annual Report - Conference on Electrical Insulation and Dielectric Phenomena, CEIDP*, 2006, pp. 668–671.

3 Z. Hanani, E. H. Ablouh, M. 'barek Amjoud, D. Mezzane, S. Fourcade and M. Gouné, *Ceram. Int.*, 2018, **44**, 10997–11000.

4 Z. Hanani, E. H. Ablouh, S. Merselmiz, J. Ghanbaja, M. Amjoud, D. Mezzane, A. Alimoussa, M. Lahcini, M. Spreitzer, D. Vengust, M. El Marssi, I. A. Luk'yanchuk, Z. Kutnjak and M. Gouné, *CrystEngComm*, 2021, **23**, 5249–5256.

5 Z. Hanani, E. H. Ablouh, M. 'barek Amjoud, D. Mezzane, S. Fourcade and M. Gouné, *Ceram. Int.*, 2018, **44**, 10997–11000.

6 Z. Hanani, S. Merselmiz, A. Danine, N. Stein, D. Mezzane, M. Amjoud, M. Lahcini, Y. Gagou, M. Spreitzer, D. Vengust, Z. Kutnjak, M. El Marssi, I. A. Luk'yanchuk and M. Gouné, *J. Adv. Ceram.*, 2020, **9**, 210–219.

7 C. C. Li, S. J. Chang, J. T. Lee and W. S. Liao, *Colloids Surfaces A Physicochem. Eng. Asp.*, 2010, **361**, 143–149.

8 M. N. Almadhoun, U. S. Bhansali and H. N. Alshareef, *J. Mater. Chem.*, 2012, **22**, 11196.

9 J. Li, K. Inukai, A. Tsuruta, Y. Takahashi and W. Shin, *J. Asian Ceram. Soc.*, 2017, **5**, 444–451.

10 W. Xia, Y. Yin, J. Xing and Z. Xu, *Results Phys.*, 2018, **11**, 877–884.

11 K. Wang, J. Fu, S. Wang, M. Gao, J. Zhu, Z. Wang and Q. Xu, *J. Colloid Interface Sci.*, 2018, **516**, 263–273.

12 Y. Wang and Z. Peng, *J. Ceram. Soc. Japan*, 2014, **122**, 719–724.

13 S. K. Singh, P. Anthony and A. Chowdhury, *Orient. J. Chem.*, 2018, **34**, 1984–1990.

14 L. Zhang, S. Lv, C. Sun, L. Wan, H. Tan and Y. Zhang, *Polymers (Basel).*, 2017, **9**, 591.

15 S. Jiang, L. Jin, H. Hou and L. Zhang, in *Polymer-Based Multifunctional Nanocomposites and Their Applications*, Elsevier, 2018, pp. 201–243.

16 S. Merselmiz, Z. Hanani, D. Mezzane, M. Spreitzer, A. Bradeško, D. Fabijan, D. Vengust, M. Amjoud, L. Hajji, Z. Abkhar, A. G. Razumnaya, B. Rožič, I. A. Luk'yanchuk and Z. Kutnjak, *Ceram. Int.*, 2020, **46**, 23867–23876.

17 K. Deshmukh, M. Basheer Ahamed, R. R. Deshmukh, S. K. Khadheer Pasha, P. R. Bhagat and K. Chidambaram, in *Biopolymer Composites in Electronics*, Elsevier, 2017, pp. 27–128.

18 T. F. Zhang, X. G. Tang, Q. X. Liu, Y. P. Jiang, X. X. Huang and Q. F. Zhou, *J. Phys. D. Appl. Phys.*, 2016, **49**, 095302.

19 Z. Wang, T. Wang, C. Wang and Y. Xiao, *J. Mater. Sci.*, 2017, **52**, 11496–11505.

20 O. Wiener, *Zur theorie der refraktionskonstanten*, Leipzig Ber., 1910.

21 K. Golden, *J. Mech. Phys. Solids*, 1986, **34**, 333–358.

22 L. Jylhä, J. Honkamo, H. Jantunen and A. Sihvola, *J. Appl. Phys.*, 2005, **97**, 104104.

23 Z. Hanani, D. Mezzane, M. Amjoud, Y. Gagou, K. Hoummada, C. Perrin, A. G. Razumnaya, Z. Kutnjak, A. Bouzina, M. El Marssi, M. Gouné and B. Rožič, *J. Mater. Sci. Mater. Electron.*, 2020, **31**, 10096–10104.

24 Y. Cheng, X. Chen, K. Wu, S. Wu, Y. Chen and Y. Meng, *J. Appl. Phys.*, 2008, **103**, 034111.

25 J. C. Maxwell Garnett, *Philos. Trans. R. Soc. London. Ser. A, Contain. Pap. a Math. or Phys. Character*, 1904, **203**, 385–420.

26 L. Jylhä and A. Sihvola, *J. Phys. D. Appl. Phys.*, 2007, **40**, 4966–4973.

27 V. A. Markel, *J. Opt. Soc. Am. A*, 2016, **33**, 1244.

28 H. Kang and G. W. Milton, *Arch. Ration. Mech. Anal.*, 2008, **188**, 93–116.

29 A. Moroz, *J. Opt. Soc. Am. B*, 2009, **26**, 517.

30 A. Sihvola, *J. Nanomater.*, 2007, **2007**, 1–9.